catalysts

MDPI

Article

Thickness-Dependent Photocatalysis of Ultra-Thin MoS_2 Film for Visible-Light-Driven CO_2 Reduction

Yi-Fan Huang [1,†], Kuan-Wei Liao [2,3,†], Fariz Rifqi Zul Fahmi [2,4,†], Varad A. Modak [1,5,6], Shang-Hsuan Tsai [2,4], Shang-Wei Ke [2,3], Chen-Hao Wang [4], Li-Chyong Chen [2,7,*] and Kuei-Hsien Chen [1,2,3,*]

1 Institute of Atomic and Molecular Sciences, Academia Sinica, Taipei 10617, Taiwan; yifanhuang1979@gmail.com (Y.-F.H.); vmodak97@gmail.com (V.A.M.)
2 Center for Condensed Matter Sciences, National Taiwan University, Taipei 10617, Taiwan; fly1299sky@gmail.com (K.-W.L.); farizrifqi49@gmail.com (F.R.Z.F.); danny458962@gmail.com (S.-H.T.); qazasdfgh28@gmail.com (S.-W.K.)
3 Department of Chemistry, National Taiwan Normal University, Taipei 11677, Taiwan
4 Department of Materials Science and Engineering, National Taiwan University of Science and Technology, Taipei 10617, Taiwan; chwang@mail.ntust.edu.tw
5 International Graduate Program of Molecular Science and Technology, National Taiwan University (NTU-MST), Taipei 10617, Taiwan
6 Molecular Science and Technology Program, Taiwan International Graduate Program (TIGP), Academia Sinica, Taipei 11529, Taiwan
7 Center of Atomic Initiative for New Materials, National Taiwan University, Taipei 10617, Taiwan
* Correspondence: chenlc@ntu.edu.tw (L.-C.C.); chenkh@pub.iams.sinica.edu.tw (K.-H.C.)
† These authors contributed equally.

check for updates

Citation: Huang, Y.-F.; Liao, K.-W.; Fahmi, F.R.Z.; Modak, V.A.; Tsai, S.-H.; Ke, S.-W.; Wang, C.-H.; Chen, L.-C.; Chen, K.-H. Thickness-Dependent Photocatalysis of Ultra-Thin MoS_2 Film for Visible-Light-Driven CO_2 Reduction. *Catalysts* **2021**, *11*, 1295. https://doi.org/10.3390/catal11111295

Academic Editors: Tilak Das and Dhanya Puthusseri

Received: 30 September 2021
Accepted: 25 October 2021
Published: 27 October 2021

Abstract: The thickness of transition metal dichalcogenides (TMDs) plays a key role in enhancing their photocatalytic CO_2 reduction activity. However, the optimum thickness of the layered TMDs that is required to achieve sufficient light absorption and excellent crystallinity has still not been definitively determined. In this work, ultra-thin molybdenum disulfide films (MoS_2TF) with 25 nm thickness presented remarkable photocatalytic activity, and the product yield increased by about 2.3 times. The photocatalytic mechanism corresponding to the TMDs' thickness was also proposed. This work demonstrates that the thickness optimization of TMDs provides a cogent direction for the design of high-performance photocatalysts.

Keywords: thickness optimization; transition metal dichalcogenides; ultra-thin molybdenum disulfide film; photocatalytic activity

1. Introduction

Photocatalytic CO_2 reduction reaction (PC-CO_2RR) is an elegant pathway in heterogeneous catalysis that transforms the CO_2 molecule, which is a widely known pollutant and one of the major causes of global warming, into a variety of useful chemicals by solar light-driven conversion [1,2], and it is also expected to help achieve the goal of net-zero industrial emissions [3]. However, the materials that have so far been investigated under the PC-CO_2RR principle still show poor conversion efficiencies and are still far from satisfying practical applications [4]. One of the main issues is the lack of high efficiency in photocatalysts that can be engaged in CO_2 reduction. Although a large number of metal oxide-based catalysts that can respond to ultraviolet light (such as titanium dioxide (TiO_2)) have been reported to be suitable for PC-CO_2RR applications, most of these materials still possess relatively low conversion efficiencies [5,6]. Consequently, researchers have devoted a great deal of time and effort to developing visible-light-active photocatalysts with appreciable conversion efficiencies [7,8]. In addition to the issue of the absorption of a broad range of wavelengths present in sunlight, another major factor that enhances the performance of a photocatalyst is the ability of excellent carrier separation and transportation. Presently, the conundrum faced by researchers in this field is that the low

charge separation efficiency of the photocatalyst leads to the rapid recombination of photogenerated electrons (e^-) and holes (h^+) in the entire photocatalytic process, making the conversion efficiency very poor [9]. Therefore, a myriad of strategies have been explored to manipulate the catalyst's charge transfer and/or spatial separation capabilities to obtain higher catalytic activity [7–10], including doping [11], co-catalysts, reduced particle size, and heterojunctions.

Two-dimensional transition metal dichalcogenide (TMD)-based catalysts have been predicted to be promising candidates for improving photocatalytic hydrogen evolution and CO_2 conversion efficiency in recent times [7,12,13], with several glowing mentions of layered molybdenum disulfide (MoS_2). Many reports indicate that MoS_2 shows great promise as a catalyst due to its tunable optical characteristics, suitable band-gap potential, and high stability under continuous light illumination, allowing it to perform visible-light photocatalysis [7,12–14]. For instance, MoS_2 exhibits a good ability to convert CO_2 into valuable fuels (CH_4, CO, CH_3OH, HCOOH) through PC-CO_2RR [15]. As a visible light-driven photocatalyst for PC-CO_2RR processes, it is necessary to conduct a thorough and systematic study of the changes in light absorption and charge recombination caused by tuning the number of layers of MoS_2 and the subsequent photocatalytic activity. It has been widely reported that a controlled number layers of MoS_2 nanosheets can be made by mechanical and chemical exfoliation methods [16,17]. When the size of MoS_2 nanosheets is reduced, it will not only change the ratio of the length of the edge to the base surface of the MoS_2 nanosheets but will also change the surface chemistry [16,17] of the material. In the past, many publications have reported that the edge sites in MoS_2 are more active than the basal plane (which is relatively inert) [17,18], with respect to catalytic activity. Therefore, it is understandably challenging to choose a method of MoS_2 production that can avoid excessive edge exposure while only tuning the number of layers in the catalyst to solve the above-mentioned problems. The surface properties and edge size of the thin film-type photocatalyst can remain unchanged when the film thickness changes. In this way, the influence of thickness on the overall catalytic performance can be isolated from other convoluting factors.

In this study, we have successfully synthesized ultra-thin MoS_2 films (MoS_2TFs) with different thicknesses as model catalysts and investigated their PC-CO_2RR activities under visible light. We demonstrated that the layer numbers and crystallinity of MoS_2TFs can be fine-tuned by a three-step post-sulfurization and chemical vapor deposition process. The results indicate that the photocatalytic activity was significantly enhanced with the increasing thickness of the MoS_2TFs. Impressively, 25 nm MoS_2TFs exhibit the highest photocatalytic activity because they have excellent optical absorption and an appropriate grain size. This strategy not only provides a new perspective for enhancing photocatalytic activity by controlling the thickness of the film but also gives us a deeper understanding of the mechanism of optical absorption and charge separation in promising layered photocatalysts such as MoS_2.

2. Results and Discussion

2.1. Synthesis of Photocatalytic Ultra-Thin Film

In this paper, we report the growth and characterization of MoS_2TFs on sapphire substrates, wherein we used thermal evaporation in combination with chemical vapor to synthesize the thin films to be studied. This method is similar to the one that was reported in our previous publication [19]. Herein, we provide a detailed report on the actual preparation of the MoS_2TFs. We also elaborate upon the methods that can be utilized to control and identify the disorder that could be observed in the thin film that we synthesized. Figure 1a depicts the schematic diagram of the three-step method proposed in this study. The first step is the deposition of the precursor MoO_3 film on the c-sapphire substrate by thermal evaporation. MoO_3 films prepared by thermal evaporation have the distinct advantages of adjustable thickness, large area, continuous film growth, good uniformity, and high quality. The second step involves annealing the MoO_3 film using a

gaseous mixture of Ar and H_2 at 500 °C for a total duration of 1 h. In this step, the MoO_3 film underwent partial reduction and was converted to an MoO_2 film, which is a form that is easier to convert to our target MoS_2TFs. The final step is the sulfurization of the MoO_2 films using a gaseous mixture of Ar and H_2S at 900 °C for 0.5 h to produce the target product (MoS_2TFs). Figure 1b shows the temperature profile of the MoS_2TFs growth process for hydrogenation and sulfurization steps. Figure 1c shows the optical photographs of the c-sapphire substrate before and after the growth of MoS_2 thin films. From this picture, it can be clearly seen that the MoS_2TFs fully cover the entire sapphire substrate and have excellent uniformity. In addition, the color of the sample surface changes from transparent to dark yellow, as there is an increase in film thickness.

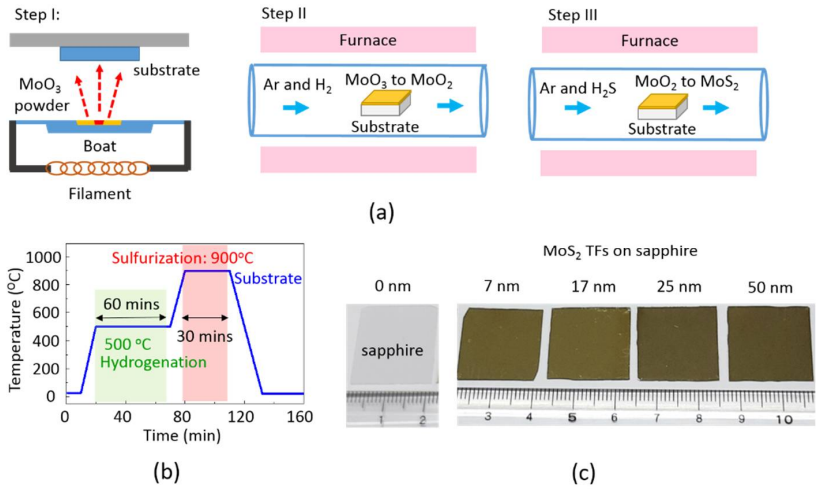

Figure 1. (**a**) Schematic diagram of the MoS_2TFs synthesis process. (**b**) The temperature profile for the MoS_2TFs growth process at different stages. (**c**) From left to right: the photographs of the substrate before and after MoS_2TFs growth with thicknesses varying from 0 to 50 nm.

2.2. Characterization of Photocatalytic Ultra-Thin Film

Figure 2a–d illustrate the thicknesses and surface roughness of the MoS_2TFs measured by atomic force microscopy. All specimens for the thickness measurements were prepared by scratching the TFs. The area that was scanned in the AFM measurements is 10 × 10 µm for these MoS_2TF samples (see the first column in Figure 2). The height profiles of the AFM images (second column in Figure 2) show that the thickness of the four MoS_2TFs samples was 7, 17, 25, and 50 nm, respectively. In addition, the surface roughness (Rq value) of the four MoS_2TFs samples was between 0.5 and 2.7 nm (third column in Figure 2). From these AFM results, it can be conclusively stated that the MoS_2TFs prepared by this three-step method are layer-controlled, have excellent homogeneity, and have very smooth surfaces.

Confocal Raman spectroscopy was used to further characterize the quality and uniformity of synthesized MoS_2TFs with various thicknesses. Figure 3 shows the Raman spectra of the 25 nm MoS_2TFs on sapphire substrates synthesized under different reaction temperatures of 500 °C, 700 °C, and 900 °C, respectively. Figure 3a shows the two main characteristic Raman peaks of MoS_2 for all of the MoS_2TFs samples, namely the in-plane E^1_{2g} peak at ≈384 cm^{-1} and the out-of-plane A_{1g} peak at ≈409 cm^{-1}. In addition, a small LA(M) sub-peak at ≈227 cm^{-1} related to the defects in MoS_2 can also be observed, which is attributed to the longitudinal phonons at the M point in the Brillouin zone [20–22]. The peak at 418 cm^{-1} comes from the sapphire substrate (A_{1g} mode) [23]. Furthermore, the intensity ratio of the LA(M) sub-peak to the A_{1g} peak can be considered to be a marker for evaluating the quality of MoS_2TFs. In general, the good quality MoS_2 samples with lower disorder can be determined by lower LA(M)/A_{1g} values [24,25]. In order to elucidate our point, we plotted the LA(M) to A_{1g} peak intensity ratio of the MoS_2TFs samples as a function of the reaction temperature, as shown in Figure 3b. The result shows that when the reaction temperature increases (from T = 500 to 700 °C), the LA(M)/A1g intensity ratio

shows a downward trend (from 0.15 down to 0.1). No clear LA(M) peak was identified as the reaction temperature approaches 900 °C (Figure 3a). To the best of our knowledge, in comparison to previous studies [24,25], the LA(M) to A1g peak intensity ratios reported in this study are the lowest values to date. These data clearly indicate that the MoS_2TFs samples grown by the high-temperature process described herein have better film quality.

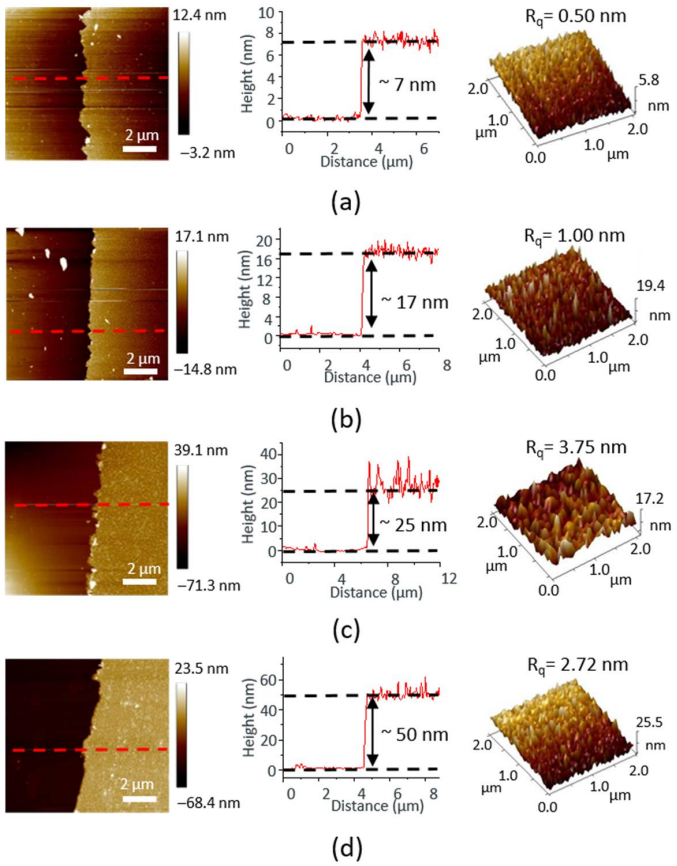

Figure 2. The AFM images (first column), height profiles (second column), and surface roughness (third column) of MoS_2TFs on a sapphire substrate with different thickness: (**a**) 7 nm, (**b**) 17 nm, (**c**) 25 nm, and (**d**) 50 nm, respectively. The thickness of MoS_2TFs was measured along the marked red lines.

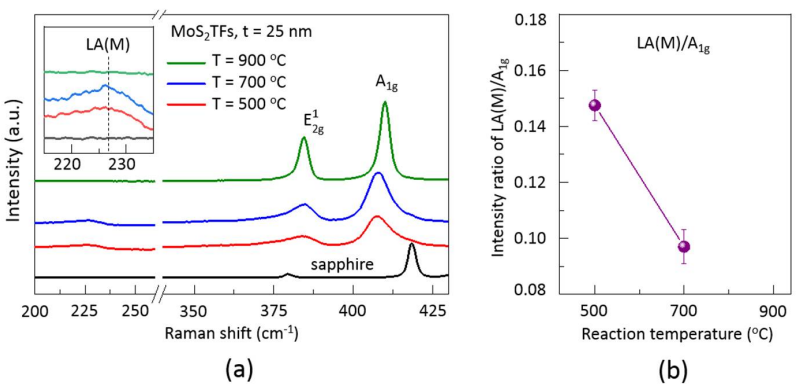

Figure 3. (**a**) Raman spectra of the 25 nm MoS_2TFs on sapphire substrates as a function of the reaction temperature using 532 nm laser for sample excitation. The inset figure shows the Raman peak position of the LA(M) mode at 227 cm^{-1}. (**b**) The LA(M) to A1g peak intensity ratio of MoS_2TFs with different reaction temperatures. No clear LA(M) mode can be found in the Raman spectrum of the T = 900 °C MoS_2TF sample (green color).

Figure 4a presents the typical Raman spectra of the prepared MoS_2TFs with thicknesses increasing from 7 to 50 nm. The Raman spectra of commercial monolayer MoS_2 on sapphire substrate and bulk MoS_2 crystal is also shown in Figure 4a, for ease of comparison. Raman spectra of the monolayer MoS2 clearly showed the two characteristic peaks at 406.5 cm^{-1} (A_{1g} mode) and 386.1 cm^{-1} ($E1_{2g}$ mode). The separation between these two peaks (A_{1g} and $E1_{2g}$ modes) is 20.4 cm^{-1}. According to previous reports [20,21], the frequency difference between the two main modes (Δk) could be used to identify the number of MoS2 layers. When the number of MoS2 layers increases, the $E1_{2g}$ mode will display a red-shift, whereas the A_{1g} mode undergoes a blue-shift [20,21]. It is worth noting that the incremental shift becomes smaller and smaller as the number of layers increases. When the number of MoS2 layers increases, the $E1_{2g}$ mode will display a red-shift, whereas the A_{1g} mode undergoes a blue-shift [20,21]. It is worth noting that the incremental shift becomes smaller and smaller as the number of layers increases. When the number of MoS_2 layers is four or more, the frequencies of these two modes will approach the values for bulk MoS_2 [26]. In Figure 4a, we can clearly observe that when the MoS2TF thickness increases from 7 nm up to 50 nm, there is no main peak shift phenomenon that is apparent in the Raman spectra of these MoS_2 samples, i.e., the two main Raman peaks (A1g and E12g modes) of these MoS2TF samples were observed at ~410 cm^{-1} and ~384 cm^{-1}, respectively. In addition, we also found that the two main Raman peak positions for all MoS2TF samples are close to the Raman peaks of commercial bulk MoS_2 crystals, and there is a slight shift (MoS_2TFs has a blue shift (~1 cm^{-1}) compared to the bulk MoS_2), as shown in Figure 4b. It is worth noting that the few-Layer MoS_2 films (4 to 6 layers) synthesized by mechanical exfoliation didn't present this slight shift phenomenon [26]. We assume it may be related to the fact that MoS_2TF is grown on sapphire substrates, instead of being directly peeled off from the bulk MoS_2 crystal. In addition, it has been reported that due to factors inherent to the substrate (such as, deformations and mismatch in the coefficient of thermal expansion), the single-layer and double-layer TMD materials will generate strain, which causes these two Raman modes to shift slightly [27,28]. The detailed mechanism of the onset of shifts in the Raman peaks in multilayer MoS2 or the ultra-thin films synthesized by us on sapphire substrates is still unclear, and further investigation is needed.

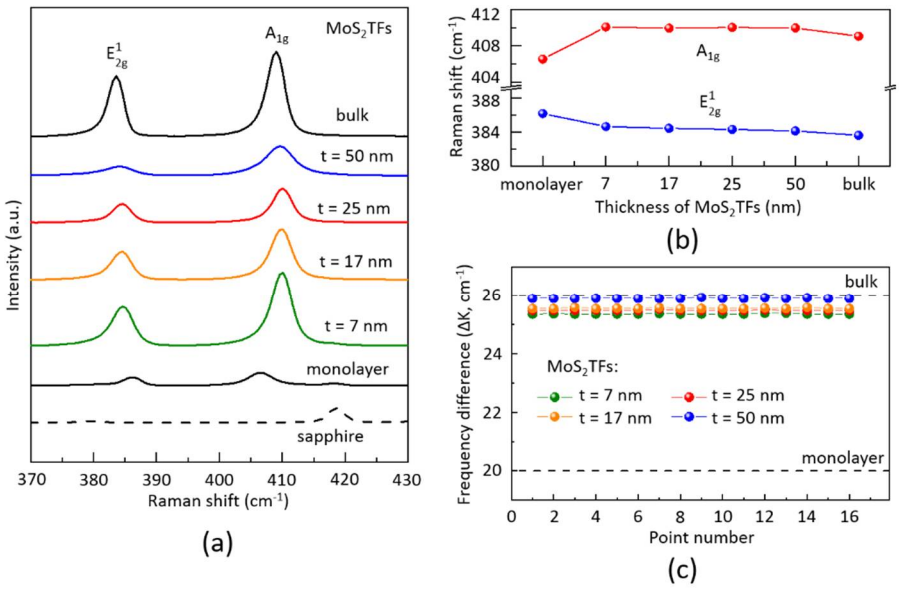

Figure 4. (**a**) Raman spectra of MoS_2TFs with thickness increasing from 7 to 50 nm. (**b**) Raman shift of A_{1g} and E^1_{2g} peak as a function of MoS_2TFs thickness. (**c**) The frequency difference between the A_{1g} and E^1_{2g} of the 16 different points on MoS_2TFs as a function of the thickness. The Raman spectra of sapphire substrate, commercial monolayer, and bulk MoS_2 have been used as reference.

In order to evaluate the uniformity of the MoS_2TFs prepared by our process, we measured the Δk value at 16 different points on the MoS_2TFs with increasing thickness, as shown in Figure 4c. The results show that the measured Δk values of all MoS_2TF samples are between 25.4 to 25.9, which are close to the values of bulk MoS_2 crystals. This result demonstrates the excellent uniformity of our custom-grown MoS_2TFs with various thicknesses. All Raman results also indicate that uniform thickness-controlled MoS_2TFs can have the advantage of large scalability of growth on sapphire substrate.

Evolution of the optical properties of the as-prepared MoS_2TFs was further investigated by measuring the optical absorbance spectra of MoS_2TFs as a function of thickness. Figure 5a shows the UV-Vis-NIR absorption spectra of 7, 17, 25, and 50 nm MoS_2TFs, respectively. All deposited films exhibit four prominent peaks characteristically indicating 2H-MoS_2 excitonic features in the visible wavelength region. More specifically, the A and B excitons that form at the K-point of the Brillouin zone appeared in the 600 to 700 nm wavelength region, while the C and D excitonic peaks were located in the wavelength range from 400 to 450 nm. The absorption spectrum of the sapphire substrate has been shown in Figure 5a. Looking at Figure 5b we found that with increasing thickness of MoS_2TFs from 7 to 25 nm, the absorbance at peak of A exciton increased rapidly from 0.25 to 0.6. However, when the film thickness increased to 50 nm, the MoS_2TFs showed a saturation trend of absorbance, similar to the absorbance spectrum of 25 nm film. The absorbance at peak of B exciton presents a trend similar to the A exciton. We also observed that the A exciton energy (E_A) of MoS_2TFs on sapphire samples will decrease as film thickness increase (from 1.851 eV to 1.834 eV), and it will converge when the thickness reaches 25 nm (about 40 layers), as shown in Figure 5c. It is worth noting that these results are not the same as previously reported in literature [29]. In a previous study, the A exciton position of the micromechanically-exfoliated nanosheets was seen to decrease from 1.89 to 1.83 eV as the thickness increases from 1 to 6 layers. When the number of layers reaches 5 or 6, the downward trend of A exciton position begins to converge. In addition, in the case of liquid-phase exfoliated nanosheet samples, when the number of layers reaches 10 layers, the exciton peak position will begin to converge. We think this may be related to the difference between the dielectric constant of the CVD-grown MoS_2TFs samples and the exfoliated samples. Since the interlayer electronic hybridization and dielectric shielding effect was changed as a function of the number of MoS_2 layers, the resulting properties of A excitons also changed comparably. However, the detailed mechanism of the position shift pertaining to the energy of the A exciton of MoS_2TFs on sapphire substrates is still unclear. Therefore, we suggest that the dielectric constant of MoS_2TFs grown on a sapphire substrate should be measured directly using spectroscopic ellipsometry combined with quantum electrostatic heterostructure (QEH) model calculation [29]. This approach can help to elucidate the layer-related exciton effect of MoS_2TFs more quantitatively.

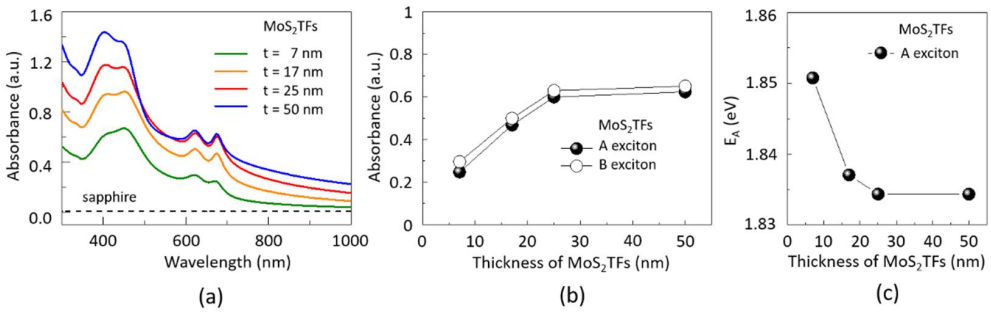

Figure 5. (**a**) UV-Vis-NIR absorption spectra of the MoS_2TFs on sapphire as a function of absorbance with thickness. (**b**) Absorbance at the peak position of A and B excitons of the MoS2 TFs as a function of thickness. (**c**) Plot of A exciton energy (EA) from absorbance as a function of MoS_2TFs thickness.

The optical band gap of a photocatalyst can be calculated by the following formula: $(\alpha h\nu)^{1/n} = A(h\nu\text{-}Eg)$ [30,31]. In this equation, 'α' is the absorption coefficient, 'h' is Planck's

constant, 'υ' is the photon frequency, 'A' is a constant, and 'Eg' is the band-gap energy. The 'n' is the exponent term, which denotes the nature of the electronic transition. When n = 1/2, it signifies a direct allowed transition, and when n = 2, it represents an indirect allowed transition. According to previous reports [32], monolayer MoS_2 is a direct energy band-gap semiconductor, and an increase in the number of layers (including multi-layer, film, and bulk crystal) causes a shift of behavior to an indirect band-gap semiconductor. Not only that, the Eg value of MoS_2 will change from 1.9 eV for a monolayer to 1.2 eV for bulk crystal. Tauc plots as a function of photon energy for MoS_2TFs can be used to determine the Eg value by extrapolating the straight-line portion of the indirect electronic transitions, as shown in Figure 6. Here, we used the indirect transition value (n = 2) to calculate the Eg value of all MoS_2TF samples (Figure 6a–d). The results show that when the film thickness is increased from 7 to 50 nm, the Eg value of MoS_2TFs will decrease from 1.71 to 1.60 eV (Figure 6e). The Eg values of monolayer and bulk crystal also shown in Figure 6e for reference purposes.

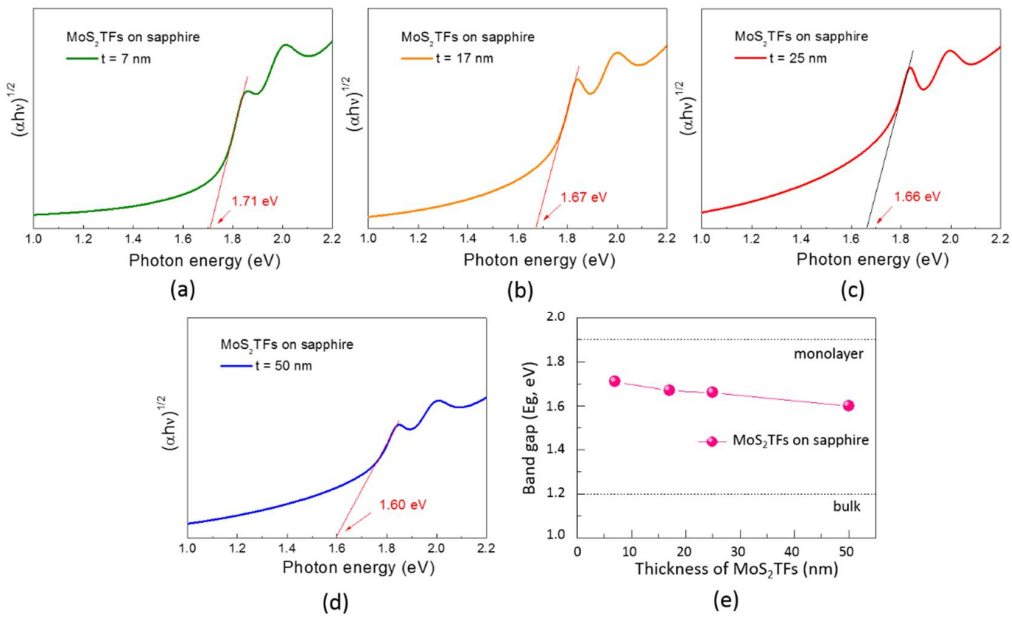

Figure 6. Tauc plots for the estimation of the band gap of MoS_2TFs on sapphire with thickness increasing from (**a**) 7 nm, (**b**) 17 nm, (**c**) 25 nm, to (**d**) 50 nm, respectively. (**e**) The band gap of MoS_2TFs as a function of thickness.

Photoluminescence (PL) is another optical spectroscopic technique used to measure the band gap of semiconductors. Monolayer MoS_2 is a direct bandgap semiconductor that exhibits significant PL intensity and prominent excitonic features (A and B exciton peaks) in PL spectra [33]. Multi-layer MoS_2 is an indirect band gap semiconductor, and its PL intensity will decrease rapidly as the number of layers increases. In bulk crystal MoS_2, the PL intensity is relatively weak; so much so, that in some cases no PL excitation at all is observable. Figure 7 shows the PL spectra of MoS_2TFs on sapphire with various thicknesses. The results show that our as-deposited MoS_2TFs do not exhibit strong PL intensity. When the thickness of MoS_2TFs is increased from 7 to 50 nm, the PL intensity will decrease dramatically (Figure 7a). No clear A exciton peak was identified in the PL spectra of 25 nm and 50 nm MoS_2TFs. The prominent MoS_2 Raman modes were observed at around 550 nm wavelength region for all MoS_2TFs samples. Not only that, the broad PL spectra profile and non-obvious excitonic features (A and B exciton peak) of the MoS_2TFs are similar to bulk crystal MoS_2 (Figure 7b). The PL signal of the sapphire substrate is still visible and overlap with A exciton peak of MoS_2 occurs at a wavelength of around 690 nm (Figure 7a,c). Therefore, it is difficult to determine the position of the A exciton peak and bandgap for all MoS_2TFs samples. The PL spectra of our as-prepared MoS_2TFs

exhibited similar excitation phenomena as chemically exfoliated MoS_2 layers. In the case of chemically exfoliated MoS_2 layers [33], when the thickness of the MoS_2 layer is greater than 7 nm, no clear A exciton peak can be observed in the PL spectrum.

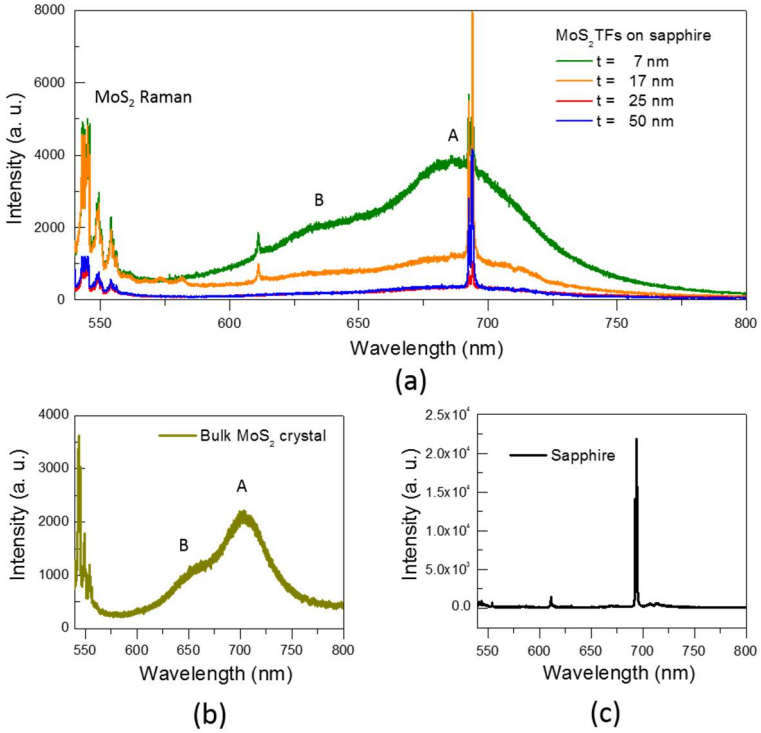

Figure 7. Photoluminescence spectra of (**a**) MoS_2 thin films grown on a sapphire substrate with different thicknesses, (**b**) sapphire, and (**c**) bulk MoS_2 crystal.

X-ray diffraction (XRD) was used to study the structural properties and crystalline parameters of the as-prepared MoS_2TFs. From the XRD patterns shown in Figure 8, it can be observed that all MoS_2TF samples are unequivocally identified as 2H MoS_2 with a strong characteristic peak appearing at $2\theta = 14.3°$, which was assigned to the MoS_2 (002) lattice plane [34]. However, the peak denoting the (004) lattice plane of MoS_2 at $2\theta = 29°$ cannot be observed in our MoS_2TF samples. Furthermore, we used the Scherrer Equation to analyse the grain size of the MoS_2TFs, as listed in Table 1. According to the Scherrer formula, $D = K\lambda/(\beta \cos \theta)$ [35], where 'D' is the average grain size in vertical direction of crystal structure, 'K' is the shape factor having a typical value of about 0.9, 'λ' is the wavelength of the X-ray source, 'β' is the full width at half maximum intensity of the peak (in Rad), and 'θ' is the Bragg angle. As seen in Figure 8b, we found that as the thickness of MoS_2TFs increased from 7 to 25 nm, the grain size of the MoS_2TFs increased from 5.6 to 21 nm. However, when the film thickness increased to 50 nm, the grain size of MoS_2TFs was constrained to around 25 nm. This data indicates that all the MoS_2TF samples have good crystallinity, and the grain size is almost identical to the measured film thickness, except in the case of the 50 nm sample.

Table 1. The calculated grain size of MoS_2TFs on sapphire from the (002) peak using Scherrer's formula.

Thickness (nm)	β/Degree	2θ/Degree	D/nm
7	1.43	14.29	5.60
17	0.64	14.47	12.51
25	0.38	14.50	21.07
50	0.32	14.47	25.02

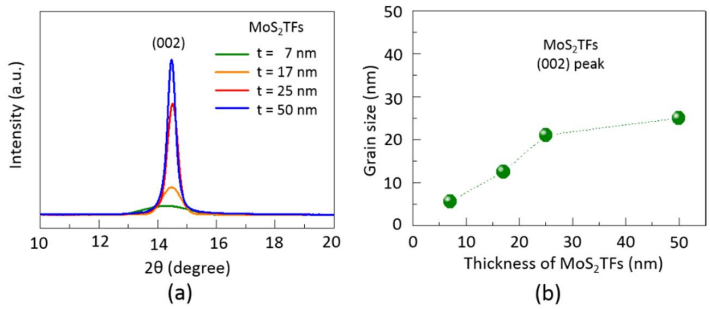

Figure 8. (**a**) XRD pattern of the MoS_2TFs on sapphire with different thicknesses. (**b**) The grain size of MoS_2TFs as a function of thickness.

2.3. Photocatalytic Performance

The evaluation of the PC-CO_2RR performance of the MoS_2TFs with various thicknesses was performed in a visible light-driven gas-phase photoreaction vessel for 24 h, as shown in Figure 9. Briefly, the MoS_2TFs with an area of 2 cm^2 were placed at the center of the photoreactor. Then, N_2 gas and moist CO_2 gas were sequentially passed through the photoreactor for 30 min and 1 h, respectively. A 100 W Xe solar simulator with an AM1.5 filter was used as the light source to study the photoconversion of CO_2 and water vapor over a time period of 24 h. The schematic representation of our gas-phase and batch-type PC-CO_2RR system is shown in Figure 9a. In order to avoid the overestimation of the catalytic activity of our samples due to carbon contamination on the surface of the reactor, we carried out two blank tests as the background for all MoS_2TF samples (Supporting Figure S1 in Supplementary Material). This background value will be subtracted from the spectral data of the final gas products produced by the MoS_2TF catalysts after 24 h of photocatalysis. Figure 9b,c show the product yields of the MoS_2TFs with different reaction temperatures and different thicknesses. All the MoS_2TFs samples are capable of catalyzing the reduction of CO_2 into methane (CH_4), ethylene (C_2H_4), acetaldehyde (CH_3CHO), and acetone (C_3H_6O). Methane and acetaldehyde were identified as the first and second major products, respectively. In addition, small amounts of ethane and acetone were also detected. The corresponding gas production yield and quantum efficiencies (QE) of all MoS_2TF samples are summarized in Tables 2 and 3, respectively.

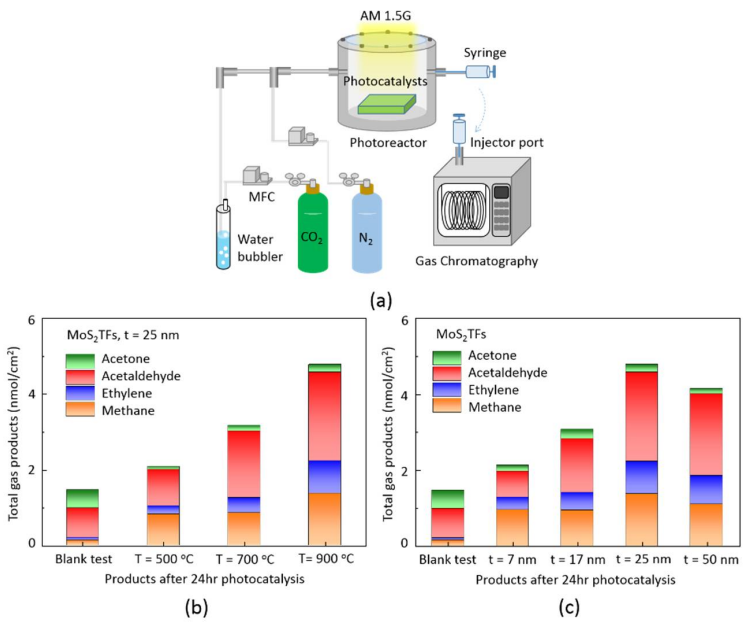

Figure 9. (**a**) Setup of gas-phase PC-CO_2RR system. The figures below that display the PC-CO_2RR activity of MoS_2TFs on sapphire with different (**b**) reaction temperatures and (**c**) different thicknesses.

Table 2. Production yields and QEs of MoS_2TFs synthesized at various reaction temperatures.

	Apparent Production Yield (nmol/cm^2)					QE (%)	
MoS_2TFs	**CH_4**	**C_2H_4**	**CH_3CHO**	**C_3H_6O**	**Total**	**MoS_2TFs**	**Total (%)**
Blank test	0.14	0.07	0.78	0.48	1.47	Blank test	none
T = 500 °C	0.83	0.22	0.96	0.08	2.09	T = 500 °C	0.000029
T = 700 °C	0.86	0.39	1.77	0.14	3.16	T = 700 °C	0.000045
T = 900 °C	1.38	0.86	2.35	0.20	4.79	T = 900 °C	0.000068

Note: The gas products from the blank test have been subtracted from all gas product values pertaining to the samples.

Table 3. Production yields and QEs of MoS_2TFs with various thicknesses.

	Apparent Production Yield (nmol/cm^2)					QE (%)	
MoS_2TFs	**CH_4**	**C_2H_4**	**CH_3CHO**	**C_3H_6O**	**Total**	**MoS_2TFs**	**Total (%)**
Blank test	0.14	0.07	0.78	0.48	1.47	Blank test	none
t = 7 nm	0.95	0.34	0.69	0.15	2.13	t = 7 nm	0.000030
t = 17 nm	0.94	0.47	1.41	0.25	3.07	t = 17 nm	0.000044
t = 25 nm	1.38	0.86	2.34	0.21	4.79	t = 25 nm	0.000068
t = 50 nm	1.10	0.75	2.16	0.15	4.16	t = 50 nm	0.000059

Note: The gas products from the blank test have been subtracted from all gas product values pertaining to the samples.

The QE of the MoS_2TFs was determined as the ratio of the effective electrons used for gas production, such as the CH_4 molecule, to the total input photon flux, and it was calculated by the following equation [36,37]:

$$\text{QE\%} = \frac{\text{Effective electrons}}{\text{Total photons}} \times 100\% = \frac{8 \times \text{Y} \times \text{N}}{\Theta \times \text{T} \times \text{S}} \times 100\% \quad (1)$$

where 'Y' is the product yield of CH_4 (mol), 'N' is Avogadro's number (6.022×10^{23} mol^{-1}), 'Θ' is the photon flux (2.46×10^{17} cm^{-2} s^{-1}), 'T' is the reaction time (s), and 'S' is the area of illumination (cm^2). The area under illumination (S) of the MoS_2TF samples is 2 cm^2. For example, the QE% of CH_4 for 25 nm MoS_2TFs after 24 h of PC-CO_2RR can be calculated as QE = $(8 \times 1.38 \times 10^{-9} \times 6.022 \times 10^{23})/(2.46 \times 10^{17} \times 24 \times 3600 \times 2) \times 100\%$ = 0.000016%. Based on the same calculation method, the QE%s of C_2H_4, CH_3CHO, and C_3H_6O for the 25 nm MoS_2TFs were calculated to be 0.000015%, 0.000033%, and 0.0000047%, respectively. The total QE of all gas products for MoS_2TFs is 0.000068%, and it is calculated by the following equation:

$$\text{Total QE\%} = \text{QE\% of } CH_4 + \text{QE\% of } C_2H_4 + \text{QE\% of } CH_3CHO + \text{QE\% of } C_3H_6O. \quad (2)$$

Figure 9b shows that the 25 nm MoS_2TFs prepared at a reaction temperature of 900 °C can convert the highest amount of CO_2 into the four gas products (total amount of gas products is 4.79 nmol/cm^2), which is followed by the samples produced at a reaction temperature of 700 °C (3.16 nmol/cm^2), and these in turn are followed by the MoS_2TF samples synthesized at a reaction temperature of 500 °C (2.09 nmol/cm^2). The resulting total QEs for the MoS_2TF samples produced at reaction temperatures of 500, 700, and 900 °C were 0.000029%, 0.000045%, and 0.000068%, respectively. In Figure 9c, we observe that as the thickness of MoS_2TFs increased from 7 to 25 nm, the gas production yield and total QE exhibited a gradually increasing trend (2.13 to 4.79 nmol/cm^2 and 0.000030 to 0.000068%). However, when the film thickness increased to 50 nm, the gas production yield and QE showed a downward trend (4.16 nmol/cm^2 and 0.000059%). These results indicate that the 25 nm MoS_2TFs exhibited the highest photocatalytic activity.

2.4. Photocatalytic Mechanism

From the above-mentioned CO_2 reduction activities of different MoS_2TF photocatalysts, we can conclude that the crystallinity and thickness of MoS_2TFs play an important

role in the PC-CO_2RR processes. We will try to understand the underlying photocatalytic mechanism from the following aspects, as illustrated in Figure 10.

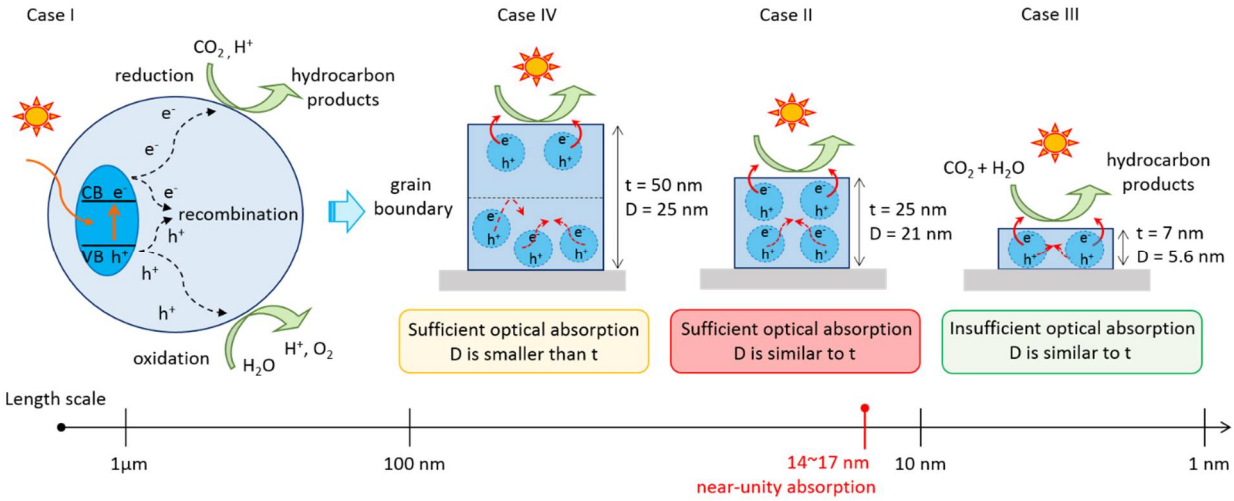

Figure 10. Schematic illustration of the proposed mechanism of ultra-thin film MoS_2 photocatalysts for visible light-driven CO_2 reduction.

2.4.1. Size Effect

In case 1 as illustrated in Figure 10, the typical process of PC-CO_2RR on a semiconductor-based photocatalyst has been schematically depicted. Briefly, the PC-CO_2RR process consists of five consecutive steps: light absorption, charge separation, CO_2 adsorption, surface redox reaction, and product desorption [38,39]. These five steps can be further divided into two theoretical categories, that is, photophysics (the first two steps) and photochemistry (the next three steps). For the purpose of understanding the performance of the catalysts we have synthesized, we will mainly focus on understanding the relationship between photophysics and the activity of our photocatalysts. The first step shows that it is necessary to analyze the ability of photocatalysts to absorb photons and consequently generate electron–hole pairs, which is acutely affected by factors such as the energy band gap (Eg) and thickness of the photocatalyst. The second step hinges on the ability of photocatalysts to effectively separate the photogenerated electrons and holes, which is directly related to charge recombination phenomena. The crystallinity and surface properties of photocatalysts all tangibly affect charge recombination. Therefore, in order to improve the overall photocatalytic efficiency, it is necessary to increase the optical absorption of the incoming visible light radiation, to generate electron–hole pairs with vigor, efficiently separate the photo-generated charge carriers, and suppress their recombination, as shown in Figure 10.

It is worth noting that the utilization of the so-called "nanosizing strategy" has proven to be very beneficial toward improving the performance of visible light-driven photocatalysts [10,40]. For instance, Ta_3N_5 nanoparticles with a particle size of 30–50 nm exhibited higher photocatalytic activity for H_2 evolution, as compared to traditional bulk Ta_3N_5 particles (300–500 nm) [40]. A photocatalyst with a smaller particle size has the advantage of a higher surface area, which also increases the density of surface catalytic sites. However, it usually results in lower crystallinity and may reduce catalytic activity. Moreover, in particle type photocatalysts with a three-dimensional geometry, calculative complications are caused by particle size reduction, such as crystal facet and morphology change. This makes it a challenging task to lucidly explain the actual catalytic mechanism. Therefore, we propose the utilization of thin-film type photocatalysts with a two-dimensional geometry to isolate the "thickness effect" and avoid the above problems for the study of specific catalytic mechanisms study.

2.4.2. Effect of Optical Absorption

According to past reports [32,41], by controlling the number of layers of MoS_2, not only can the bandgap be fine-tuned, but the light absorption performance can also be optimized. In a previous study, Atwater's group reported that the sub-15 nm thick TMD flakes created by mechanical exfoliation, have near-unity optical absorption [41]. Their calculated and measured absorption spectra showed that the ultra-thin (14–17 nm) MoS2 flakes on an Ag back reflector have the highest broadband absorption. According to our experimental data, the energy bandgap of MoS_2TF samples with different thicknesses is about 1.7 to 1.6 eV and there is not too much variation in these values (Figure 6e). However, there are obvious differences in the optical absorption of MoS2TF samples with different thicknesses (Figure 5b). The ultra-thin MoS_2TFs on sapphire with a thickness of 25 nm exhibited the highest optical absorption. This result is similar to the optical absorption capacity of MoS2 flakes reported in literature. Therefore, we believe that the sufficient optical absorption of visible light radiation by films having an optimized thickness of 25 nm (sample (case II)), which exhibits better photocatalytic activity than 7 or17 nm MoS_2TFs samples (case III), as shown in Figure 10.

2.4.3. Effect of Grain Size

According to our experimental data, the grain size of MoS_2TFs samples with different thicknesses is about 7 to 25 nm. In addition, a point to be noted is that the 25 nm MoS_2TF sample has almost the same thickness as the grain size. The 50 nm MoS_2TF sample has grain boundaries because the grain size is only 25 nm. Therefore, we propose a possible reason to explain why the 25 nm MoS_2TFs sample (case II) has better photocatalytic activity than 50 nm Mo_{S2}TFs samples (case IV), as shown in Figure 10. It is well known that the grain boundary of semiconductors is the primary site of charge recombination, and changes therein significantly affect the charge transport [42,43]. Based on this knowledge, we think it is reasonable that the grain size of ultra-thin MoS_2TFs samples is similar to film thickness (case II: D is similar to t), which can promote the internal photogenerated carriers to migrate to the surface and efficiently drive the catalytic reaction (case II). On the contrary, the grain size of thick MoS_2TFs samples is smaller than the film thickness (case IV: D is smaller than t), resulting in the formation of grain boundaries inside the film and the subsequent suppression of the probability of photogenerated carrier transfer to the surface. We studied two additional thick MoS_2TFs samples and measured their grain size and catalytic activity to support this scientific point (Supporting Figures S2 and S3 and Supporting Table S1). The results clearly indicate that when the thickness is continuously increased (from 40 to 60 nm) without increasing the grain size (maintained at around 20 nm), the photocatalytic activity does not increase dramatically. In our current TFs process, the biggest grain size of MoS_2TFs with a thickness of 7 to 60 nm is about 20 nm, and the 25 nm MoS_2TFs sample has the best photocatalytic activity of about 4.79 nmol/cm^2. Therefore, we believe that in addition to light absorption, the grain boundary inside the photocatalyst is another important factor that significantly affects the catalytic activity.

2.4.4. Stability Test

In order to test the stability of our MoS_2TFs, this model catalyst was reused in a fresh reactor for three successive cycles. According to Supporting Figure S4, the total gas production yield slightly decreases over time, and the reduced ratio was calculated to be about 10% after three cycles. The slight decrease in the activity after the three cycles might be due to the inactivation or poisoning of the catalytic sites on the basal plane MoS_2TFs. In addition, we also found a slight change in the production ratio of methane and acetaldehyde (methane production is increased and acetaldehyde formation is decreased). The results indicated that when reducing the catalytic sites on the MoS_2TFs surface, the catalytic activity and the reaction pathway of the product will be consequently altered. The detailed reaction mechanism is still unclear, and further investigation is needed.

In addition to optical absorption and the grain size of the MoS_2TFs, other related phenomena worth studying further include measuring the photocarrier recombination losses, surface reaction investigations, product analysis, and isotopic labeling. For recombination, it is worth noting that traditionally, time-resolved absorption and PL spectroscopies can successfully study the dynamic behavior of photocarriers in photocatalysis [44,45]. However, when the thickness increases, neither our as-prepared MoS_2 film nor the MoS_2 flake [29] have any obvious PL emission. Therefore, this tool cannot be used to understand the behavior of carrier recombination in the case of our MoS_2TFs. Other alternative tools need to be selected and developed, such as advanced space-resolved techniques [46]. For surface reactions, the relationship between the surface of TMD catalysts and the surface reaction pathways has still not been clearly understood. It is necessary to use in situ catalytic tools to study the surface reactions on the catalyst surface, such as ambient pressure X-ray photoelectron spectroscopy for CO_2 adsorption [47] and infrared absorption spectroscopy for surface species [48]. For product analysis, the accurate measurement of gas products relies heavily on the sensitivity and number of gas analysis detectors (such as gas chromatography-thermal conductivity detector (GC-TCD) and chromatography-flame ionization detector (GC-FID)) [49]. In most cases, only one gas detector is used, which often leads to inaccuracies in the overall gaseous product evaluation. For instance, H_2 could also be one of the products of CO_2 reduction, and its detection requires GC-TCD. Not only that, the H_2 production rate should also be factored into the quantum efficiency calculations. The complete analysis of the products of CO_2 reduction with the appropriate equipment is one of the directions that certainly must not be overlooked. While isotopic labeling technology may be a slightly more expensive alternative to confirm the accuracy of the products and product-specific active sites [50], it is certainly a project well worth being further investigated.

3. Materials and Methods

3.1. Sample Preparation

Uniform MoS_2TFs on (0001) sapphire substrate with different thicknesses were prepared by two-step post-sulfurization of vacuum-deposited molybdenum trioxide (MoO_3) films. Initially, a c-face sapphire substrate was cleaned with ethanol, acetone, and DI water for 5 min, respectively. Then, the clear substrates were subjected to O_2 plasma treatment for 10 min prior to the deposition of the MoO_3 film. The precursor MoO_3 powder was supplied by Alfa Aesar with 99.95% purity, which was deposited on the top of sapphire substrate as a thin film, using thermal evaporation. In this process, the desired thickness of the film to be deposited can be closely monitored using a quartz crystal microbalance (QCM) by measuring the change in frequency of a quartz crystal resonator. The deposition rate was maintained in the range of 0.1 to 0.2 kÅs^{-1}. Thereafter, all samples were placed into a chemical vapor deposition (CVD) system to perform the post-sulfurization process. Before introducing H_2S gas into the system, the MoO_3 films were annealed at 500 °C for 1 h under vacuum in an Ar-H_2 environment (4:1), with the aim of reducing them into MoO_2. Finally, the CVD growth process was performed at atmospheric pressure with 100 sccm of Ar and an H_2-H_2S mixture (flow rate 1:4). The post-sulfurization process was performed at 1000 °C at the rate of 30 °C min^{-1}, and this condition was maintained for 30 mins to ensure successful sulfurization of the MoS_2TFs.

3.2. Characterization

The as-grown MoS_2TFs on sapphire substrates were systematically characterized by the following microscopy and spectroscopy-based tools. Firstly, the thickness and surface roughness of MoS_2TFs was examined using the tapping mode of atomic force microscopy (AFM) with a scanning rate of 0.5 Hz and 10 μm scanning area using a Bruker Dimension Icon Atomic Force Microscope. The Raman and photoluminescence (PL) spectra were recorded on a Jobin-Yvon LabRAM H800 system with a 532 nm Nd:YAG laser as the excitation source and a spot size of ≈1 μm. In addition, the optical absorbance of

the MoS_2TFs was measured by a UV-Vis-NIR spectrophotometer (JASCO V-670). The optical band gap of the MoS_2TFs was determined using Tauc plots. After that, the crystal structure and grain size of the MoS_2TFs was determined using a Bruker D2 PHASER X-ray diffractometer.

3.3. Photocatalytic Activity Measurement

The gaseous product species generated by all the MoS_2TF photocatalysts after the PC-CO_2RR process were analyzed by gas chromatography (GC), on an Agilent 6890 system using a glass PLOT column (RT-Q-BOND), and a flame ionization detector (FID).

4. Conclusions

In summary, the lab-grown MoS_2TFs on sapphire with thickness from 7 to 50 nm were used as a model catalyst and the photocatalytic CO_2 reduction activities of thickness dependent MoS_2TFs were systematically investigated. The MoS_2TFs with 25 nm thickness exhibited the highest photocatalytic activities under visible light irradiation, corresponding to a gas production yield of 4.79 nmol/cm^2 with a QE of 0.000068%. It is demonstrated that 25 nm MoS_2TFs have the best ratio of light absorption and grain size, as compared to films of other thicknesses. We also proposed a systematic photocatalytic mechanism to relate the dependence of the thickness of TMD based photocatalysts, on their eventual catalytic mechanism. This study provides a novel outlook towards the development of high-efficiency two-dimensional material catalysts for the efficient reduction of CO_2 into other useful chemical species.

Supplementary Materials: The following are available online at https://www.mdpi.com/article/10.3390/catal11111295/s1, Figure S1: The total gas products of two kinds of blank test conditions for photocatalysis: 1.47 nmol/cm^2 for blank test-1 and 0.27 nmol/cm^2 for blank test-2, respectively, Figure S2: XRD pattern of the MoS_2TFs on sapphire with different thicknesses: (a) t = 40 nm and (b) t = 60 nm, Table S1: The calculated grain size of MoS_2TFs on sapphire from (002) peak using Scherrer's formula, Figure S3: The PC-CO_2RR activity of MoS_2TFs on sapphire with thickness increasing from 40 to 60 nm, Figure S4: The stability study of the photocatalytic CO_2 reduction over the MoS_2TFs with 25 nm thickness.

Author Contributions: Y.-F.H. conceived and designed the experiments. K.-W.L. and F.R.Z.F. carried out the thin-film deposition and material characterizations. K.-W.L., F.R.Z.F., Y.-F.H., S.-H.T., S.-W.K. and C.-H.W. performed the GC experimental setup, calibration, photocatalytic activity, and data analysis. Y.-F.H., V.A.M. and K.-H.C. co-wrote the manuscript. K.-H.C. and L.-C.C. supervised the project. All authors have read and agreed to the published version of the manuscript.

Funding: This work was financially supported by the Ministry of Science and Technology, Taiwan (Grant Numbers: 108-2119-M-002-030, 109-2123-M-002-004, 110-2123-M-002-006, and 108-2112-M-001-046-MY2) and by Academia Sinica (Grant Number AS-iMATE-110-34). Y.-F.H. acknowledges support from IAMS Junior Fellowship by Institute of Atomic and Molecular Sciences, Academia Sinica, Taiwan.

Conflicts of Interest: The authors declare no conflict of interest.

References

1. Kätelhön, A.; Meys, R.; Deutz, S.; Suh, S.; Bardow, A. Climate change mitigation potential of carbon capture and utilization in the chemical industry. *Proc. Natl. Acad. Sci. USA* **2019**, *116*, 11187–11194. [CrossRef] [PubMed]
2. Hepburn, C.; Adlen, E.; Beddington, J.; Carter, E.A.; Fuss, S.; Mac Dowell, N.; Minx, J.C.; Smith, P.; Williams, C.K. The technological and economic prospects for CO_2 utilization and removal. *Nature* **2019**, *575*, 87–97. [CrossRef]
3. Davis, S.J.; Lewis, N.S.; Shaner, M.; Aggarwal, S.; Arent, D.; Azevedo, I.L.; Benson, S.M.; Bradley, T.; Brouwer, J.; Chiang, Y.M.; et al. Net-zero emissions energy systems. *Science* **2018**, *360*, 6396. [CrossRef] [PubMed]
4. Bushuyev, O.S.; De Luna, P.; Dinh, C.T.; Tao, L.; Saur, G.; van de Lagemaat, J.; Kelley, S.O.; Sargent, E.H. What should we make with CO_2 and how can we make it? *Joule* **2018**, *2*, 825–832. [CrossRef]
5. Indrakanti, V.P.; Kubicki, J.D.; Schobert, H.H. Photoinduced activation of CO_2 on Ti-based heterogeneous catalysts: Current state, chemical physics-based insights and outlook. *Energy Environ. Sci.* **2009**, *2*, 745–758. [CrossRef]

6. Chang, X.; Wang, T.; Gong, J. CO_2 photo-reduction: Insights into CO_2 activation and reaction on surfaces of photocatalysts. *Energy Environ. Sci.* **2016**, *9*, 2177–2196. [CrossRef]
7. Voiry, D.; Shin, H.S.; Loh, K.P.; Chhowalla, M. Low-dimensional catalysts for hydrogen evolution and CO_2 reduction. *Nat. Rev. Chem.* **2018**, *2*, 0105. [CrossRef]
8. Djurišić, A.B.; He, Y.; Ng, A.M. Visible-light photocatalysts: Prospects and challenges. *APL Mater.* **2020**, *8*, 030903–030924. [CrossRef]
9. Marszewski, M.; Cao, S.; Yu, J.; Jaroniec, M. Semiconductor-based photocatalytic CO_2 conversion. *Mater. Horiz.* **2015**, *2*, 261–278. [CrossRef]
10. Maeda, K. Photocatalytic water splitting using semiconductor particles: History and recent developments. *J. Photochem. Photobiol. C Photochem. Rev.* **2011**, *12*, 237–268. [CrossRef]
11. Arumugam, M.; Tahir, M.; Praserthdam, P. Effect of nonmetals (B, O, P, and S) doped with porous g-C_3N_4 for improved electron transfer towards photocatalytic CO_2 reduction with water into CH_4. *Chemosphere* **2021**, *286*, 131765. [CrossRef]
12. Bi, W.; Wu, C.; Xie, Y. Atomically thin two-dimensional solids: An emerging platform for CO_2 electroreduction. *ACS Energy Lett.* **2018**, *3*, 624–633. [CrossRef]
13. Hasani, A.; Tekalgne, M.; Van Le, Q.; Jang, H.W.; Kim, S.Y. Two-dimensional materials as catalysts for solar fuels: Hydrogen evolution reaction and CO_2 reduction. *J. Mater. Chem. A* **2019**, *7*, 430–454. [CrossRef]
14. Yu, S.; Wu, X.; Wang, Y.; Guo, X.; Tong, L. 2D materials for optical modulation: Challenges and opportunities. *Adv. Mater.* **2017**, *29*, 1606128. [CrossRef]
15. Singh, S.; Modak, A.; Pant, K.K.; Sinhamahapatra, A.; Biswas, P. MoS_2–Nanosheets-based catalysts for photocatalytic CO_2 reduction: A review. *ACS Appl. Nano Mater.* **2021**, *4*, 8644–8667. [CrossRef]
16. Chhowalla, M.; Shin, H.S.; Eda, G.; Li, L.J.; Loh, K.P.; Zhang, H. The chemistry of two-dimensional layered transition metal dichalcogenide nanosheets. *Nat. Chem.* **2013**, *5*, 263–275. [CrossRef]
17. Wang, H.; Liu, X.; Niu, P.; Wang, S.; Shi, J.; Li, L. Porous two-dimensional materials for photocatalytic and electrocatalytic applications. *Matter* **2020**, *2*, 1377–1413. [CrossRef]
18. Jaramillo, T.F.; Jørgensen, K.P.; Bonde, J.; Nielsen, J.H.; Horch, S.; Chorkendorff, I. Identification of active edge sites for electrochemical H_2 evolution from MoS_2 nanocatalysts. *Science* **2007**, *317*, 100–102. [CrossRef]
19. Lin, Y.K.; Chen, R.S.; Chou, T.C.; Lee, Y.H.; Chen, Y.F.; Chen, K.H.; Chen, L.C. Thickness-dependent binding energy shift in few-layer MoS_2 grown by chemical vapor deposition. *ACS Appl. Mater. Interfaces* **2016**, *8*, 22637–22646. [CrossRef]
20. Wu, J.B.; Lin, M.L.; Cong, X.; Liu, H.N.; Tan, P.H. Raman spectroscopy of graphene-based materials and its applications in related devices. *Chem. Soc. Rev.* **2018**, *47*, 1822–1873. [CrossRef]
21. Ye, M.; Winslow, D.; Zhang, D.; Pandey, R.; Yap, Y.K. Recent advancement on the optical properties of two-dimensional molybdenum disulfide (MoS_2) thin films. *Photonics* **2015**, *2*, 288–307. [CrossRef]
22. Mignuzzi, S.; Pollard, A.J.; Bonini, N.; Brennan, B.; Gilmore, I.S.; Pimenta, M.A.; Richards, D.; Roy, D. Effect of disorder on Raman scattering of single-layer. *Phys. Rev. B* **2015**, *91*, 195411. [CrossRef]
23. Feng, Z.C.; Schurman, M.; Stall, R.A. How to distinguish the Raman modes of epitaxial GaN with phonon features from sapphire substrate—Comments on "Optical properties of GaN film grown by metalorganic chemical vapor deposition" [J. Vac. Sci. Technol. A 14, 840 (1996)]. *J. Vac. Sci. Technol. A Vac. Surf. Films* **1997**, *15*, 2428–2430. [CrossRef]
24. Mercado, E.; Goodyear, A.; Moffat, J.; Cooke, M.; Sundaram, R.S. A Raman metrology approach to quality control of 2D MoS_2 film fabrication. *J. Phys. D Appl. Phys.* **2017**, *50*, 184005. [CrossRef]
25. Zhong, W.; Deng, S.; Wang, K.; Li, G.; Li, G.; Chen, R.; Kwok, H.S. Feasible route for a large area few-layer MoS_2 with magnetron sputtering. *Nanomaterials* **2018**, *8*, 590. [CrossRef]
26. Lee, C.; Yan, H.; Brus, L.E.; Heinz, T.F.; Hone, J.; Ryu, S. Anomalous lattice vibrations of single-and few-layer MoS2. *ACS Nano* **2010**, *4*, 2695–2700. [CrossRef]
27. Pak, S.; Lee, J.; Lee, Y.W.; Jang, A.R.; Ahn, S.; Ma, K.Y.; Cho, Y.; Hong, J.; Lee, S.; Jeong, H.Y.; et al. Strain-mediated interlayer coupling effects on the excitonic behaviors in an epitaxially grown MoS_2/WS_2 van der Waals heterobilayer. *Nano Lett.* **2017**, *17*, 5634–5640. [CrossRef]
28. Ahn, G.H.; Amani, M.; Rasool, H.; Lien, D.H.; Mastandrea, J.P.; Ager Iii, J.W.; Dubey, M.; Chrzan, D.C.; Minor, A.M.; Javey, A. Strain-engineered growth of two-dimensional materials. *Nat. Commun.* **2017**, *8*, 608. [CrossRef] [PubMed]
29. Synnatschke, K.; Cieslik, P.A.; Harvey, A.; Castellanos-Gomez, A.; Tian, T.; Shih, C.J.; Chernikov, A.; Santos, E.J.G.; Coleman, J.N.; Claudia Backes, C. Length-and thickness-dependent optical response of liquid-exfoliated transition metal dichalcogenides. *Chem. Mater.* **2019**, *31*, 10049–10062. [CrossRef]
30. Makuła, P.; Pacia, M.; Macyk, W. How to correctly determine the band gap energy of modified semiconductor photocatalysts based on UV–Vis spectra. *J. Phys. Chem. Lett.* **2018**, *9*, 6814–6817. [CrossRef]
31. Xu, X.; Lu, R.; Zhao, X.; Xu, S.; Lei, X.; Zhang, F.; Evans, D.G. Fabrication and photocatalytic performance of a $Zn_xCd_{1-x}S$ solid solution prepared by sulfuration of a single layered double hydroxide precursor. *Appl. Catal. B Environ.* **2011**, *102*, 147–156. [CrossRef]
32. Splendiani, A.; Sun, L.; Zhang, Y.; Li, T.; Kim, J.; Chim, C.Y.; Galli, G.; Wang, F. Emerging photoluminescence in monolayer MoS_2. *Nano Lett.* **2010**, *10*, 1271–1275. [CrossRef]

33. Eda, G.; Yamaguchi, H.; Voiry, D.; Fujita, T.; Chen, M.; Chhowalla, M. Photoluminescence from chemically exfoliated MoS_2. *Nano Lett.* **2011**, *11*, 5111–5116. [CrossRef] [PubMed]
34. Laskar, M.R.; Ma, L.; Kannappan, S.; Park, P.S.; Krishnamoorthy, S.; Nath, D.N.; Lu, W.; Wu, Y.; Rajan, S. Large area single crystal (0001) oriented MoS_2. *Appl. Phys. Lett.* **2013**, *102*, 252108. [CrossRef]
35. Patterson, A.L. The Scherrer formula for X-ray particle size determination. *Phys. Rev.* **1939**, *56*, 978. [CrossRef]
36. Zhang, H.; Liu, H.; Tian, Z.; Lu, D.; Yu, Y.; Cestellos-Blanco, S.; Sakimoto, K.K.; Yang, P. Bacteria photosensitized by intracellular gold nanoclusters for solar fuel production. *Nat. Nanotechnol.* **2018**, *13*, 900–905. [CrossRef] [PubMed]
37. Li, X.; Sun, Y.; Xu, J.; Shao, Y.; Wu, J.; Xu, X.; Pan, Y.; Ju, H.; Zhu, J.; Xie, Y. Selective visible-light-driven photocatalytic CO_2 reduction to CH_4 mediated by atomically thin $CuIn_5S_8$ layers. *Nat. Energy* **2019**, *4*, 690–699. [CrossRef]
38. Linsebigler, A.L.; Lu, G.; Yates, J.T., Jr. Photocatalysis on TiO_2 surfaces: Principles, mechanisms, and selected results. *Chem. Rev.* **1995**, *95*, 735–758. [CrossRef]
39. Wu, J.; Huang, Y.; Ye, W.; Li, Y. CO_2 reduction: From the electrochemical to photochemical approach. *Adv. Sci.* **2017**, *4*, 1700194. [CrossRef]
40. Maeda, K.; Nishimura, N.; Domen, K. A precursor route to prepare tantalum (V) nitride nanoparticles with enhanced photocatalytic activity for hydrogen evolution under visible light. *Appl. Catal. A Gen.* **2009**, *370*, 88–92. [CrossRef]
41. Jariwala, D.; Davoyan, A.R.; Tagliabue, G.; Sherrott, M.C.; Wong, J.; Atwater, H.A. Near-unity absorption in van der Waals semiconductors for ultrathin optoelectronics. *Nano Lett.* **2016**, *16*, 5482–5487. [CrossRef]
42. Samaj, L. Recombination processes at grain boundaries in polycrystalline semiconductors. *Phys. Status Solidi A* **1987**, *100*, 157–167. [CrossRef]
43. Lee, H.C.; Park, O.O. Electron scattering mechanisms in indium-tin-oxide thin films: Grain boundary and ionized impurity scattering. *Vacuum* **2004**, *75*, 275–282. [CrossRef]
44. Godin, R.; Wang, Y.; Zwijnenburg, M.A.; Tang, J.; Durrant, J.R. Time-resolved spectroscopic investigation of charge trapping in carbon nitrides photocatalysts for hydrogen generation. *J. Am. Chem. Soc.* **2017**, *139*, 5216–5224. [CrossRef]
45. Miao, T.J.; Tang, J. Characterization of charge carrier behavior in photocatalysis using transient absorption spectroscopy. *J. Chem. Phys.* **2020**, *152*, 194201. [CrossRef] [PubMed]
46. Gao, Y.; Nie, W.; Wang, X.; Fan, F.; Li, C. Advanced space-and time-resolved techniques for photocatalyst studies. *Chem. Commun.* **2020**, *56*, 1007–1021. [CrossRef] [PubMed]
47. Favaro, M.; Xiao, H.; Cheng, T.; Goddard, W.A.; Yano, J.; Crumlin, E.J. Subsurface oxide plays a critical role in CO_2 activation by Cu (111) surfaces to form chemisorbed CO_2, the first step in reduction of CO_2. *Proc. Natl. Acad. Sci. USA* **2017**, *114*, 6706–6711. [PubMed]
48. Zaera, F. New advances in the use of infrared absorption spectroscopy for the characterization of heterogeneous catalytic reactions. *Chem. Soc. Rev.* **2014**, *43*, 7624–7663. [CrossRef]
49. Chladek, P.; Coleman, L.J.; Croiset, E.; Hudgins, R.R. Gas chromatography method for the characterization of ethanol steam reforming products. *J. Chromatogr. Sci.* **2007**, *45*, 153–157. [CrossRef] [PubMed]
50. Lum, Y.; Ager, J.W. Evidence for product-specific active sites on oxide-derived Cu catalysts for electrochemical CO_2 reduction. *Nat. Catal.* **2019**, *2*, 86–93. [CrossRef]